Evidence from MESSENGER for sulfur- and carbon-driven explosive volcanism on Mercury

Shoshana Z. Weider[1], Larry R. Nittler[1], Scott L. Murchie[2], Patrick N. Peplowski[2], Timothy J. McCoy[3], Laura Kerber[4], Christian Klimczak[5], Carolyn M. Ernst[2], Timothy A. Goudge[6], Richard D. Starr[7], Noam R. Izenberg[2], Rachel L. Klima[2], and Sean C. Solomon[1,8]

[1]Department of Terrestrial Magnetism, Carnegie Institution of Washington, Washington, District of Columbia, USA, [2]The Johns Hopkins University Applied Physics Laboratory, Laurel, Maryland, USA, [3]Department of Mineral Sciences, National Museum of Natural History, Smithsonian Institution, Washington, District of Columbia, USA, [4]Jet Propulsion Laboratory, Pasadena, California, USA, [5]Department of Geology, University of Georgia, Athens, Georgia, USA, [6]Jackson School of Geosciences, University of Texas at Austin, Austin, Texas, USA, [7]Physics Department, Catholic University of America, Washington, District of Columbia, USA, [8]Lamont-Doherty Earth Observatory, Columbia University, Palisades, New York, USA

Abstract Targeted MErcury Surface, Space ENvironment, GEochemistry, and Ranging (MESSENGER) X-Ray Spectrometer measurements of Mercury's largest identified pyroclastic deposit are combined with neutron and reflectance spectroscopy data to constrain the composition of volatiles involved in the eruption that emplaced the pyroclastic material. The deposit, northeast of the Rachmaninoff basin, is depleted in S (relative to Ca and Si) and C, compared with the rest of Mercury's surface. Spectral reflectance measurements of the deposit indicate relatively high overall reflectance and an oxygen-metal charge transfer (OMCT) absorption band at ultraviolet wavelengths. These results are consistent with oxidation of graphite and sulfides during magma ascent, via reaction with oxides in the magma or assimilated country rock, and the formation of S- and C-bearing volatile species. Consumption of graphite during oxidation could account for the elevated reflectance of the pyroclastic material, and the strength of the OMCT band is consistent with ~0.03–0.1 wt % FeO in the deposit.

1. Introduction

The MErcury Surface, Space ENvironment, GEochemistry, and Ranging (MESSENGER) mission has provided abundant evidence that effusive volcanism shaped much of Mercury's surface [e.g., *Head et al.*, 2011; *Byrne et al.*, 2013; *Denevi et al.*, 2013; *Whitten et al.*, 2014]. In addition to widespread plains deposits, there is evidence for explosive volcanic deposits at a number of sites. The presence of pyroclastic deposits was first hypothesized on the basis of Mariner 10 images [e.g., *Rava and Hapke*, 1987; *Robinson and Lucey*, 1997]. Dozens of pyroclastic deposits, formed by past volcanic eruptions, were subsequently identified from multi-spectral images obtained during MESSENGER's three flybys of Mercury [e.g., *Murchie et al.*, 2008; *Head et al.*, 2008, 2009; *Kerber et al.*, 2009, 2011; *Prockter et al.*, 2010]. These deposits are characterized by high reflectance and "red" spectral slopes (i.e., the reflectance increases steeply with increasing wavelength) from ultraviolet to near-infrared wavelengths and diffuse borders [*Blewett et al.*, 2009; *Kerber et al.*, 2009, 2011]. The deposits surround scalloped, rimless pits, which are interpreted as the source vents for the eruptive deposits [*Kerber et al.*, 2011]. From the improved coverage and resolution of MESSENGER orbital data, a larger catalog of pyroclastic deposits has now been compiled [*Kerber et al.*, 2011; *Goudge et al.*, 2014; *Thomas et al.*, 2014]. The deposits are concentrated along fractures at the margins of impact basins, within impact craters, and along lobate scarps [*Goudge et al.*, 2014; *Thomas et al.*, 2015]. Among 150 pyroclastic deposits in the most recent catalog [*Thomas et al.*, 2014], the deposit to the northeast of Rachmaninoff impact basin (NE Rachmaninoff; Figure 1a) is by far the largest: its distinctive spectral signature is discerned to a maximum radial range of ~130 km [*Thomas et al.*, 2014]. This deposit also has the highest visible-wavelength reflectance on Mercury [*Murchie et al.*, 2015].

Explosive volcanism on Earth is driven primarily by the exsolution of magmatic H_2O and CO_2 [e.g., *Wallace et al.*, 2015], but the volatiles responsible for Mercury's pyroclastic activity have yet to be determined. Geochemical results from MESSENGER's orbital campaigns [*Nittler et al.*, 2011; *Peplowski et al.*, 2011, 2012, 2014, 2015, 2016; *Evans et al.*, 2012, 2015; *Weider et al.*, 2012, 2014, 2015] have revealed that Mercury's silicate fraction is highly reduced and volatile rich (i.e., with high concentrations of K, Na, Cl, S, and C). Here we present an analysis of
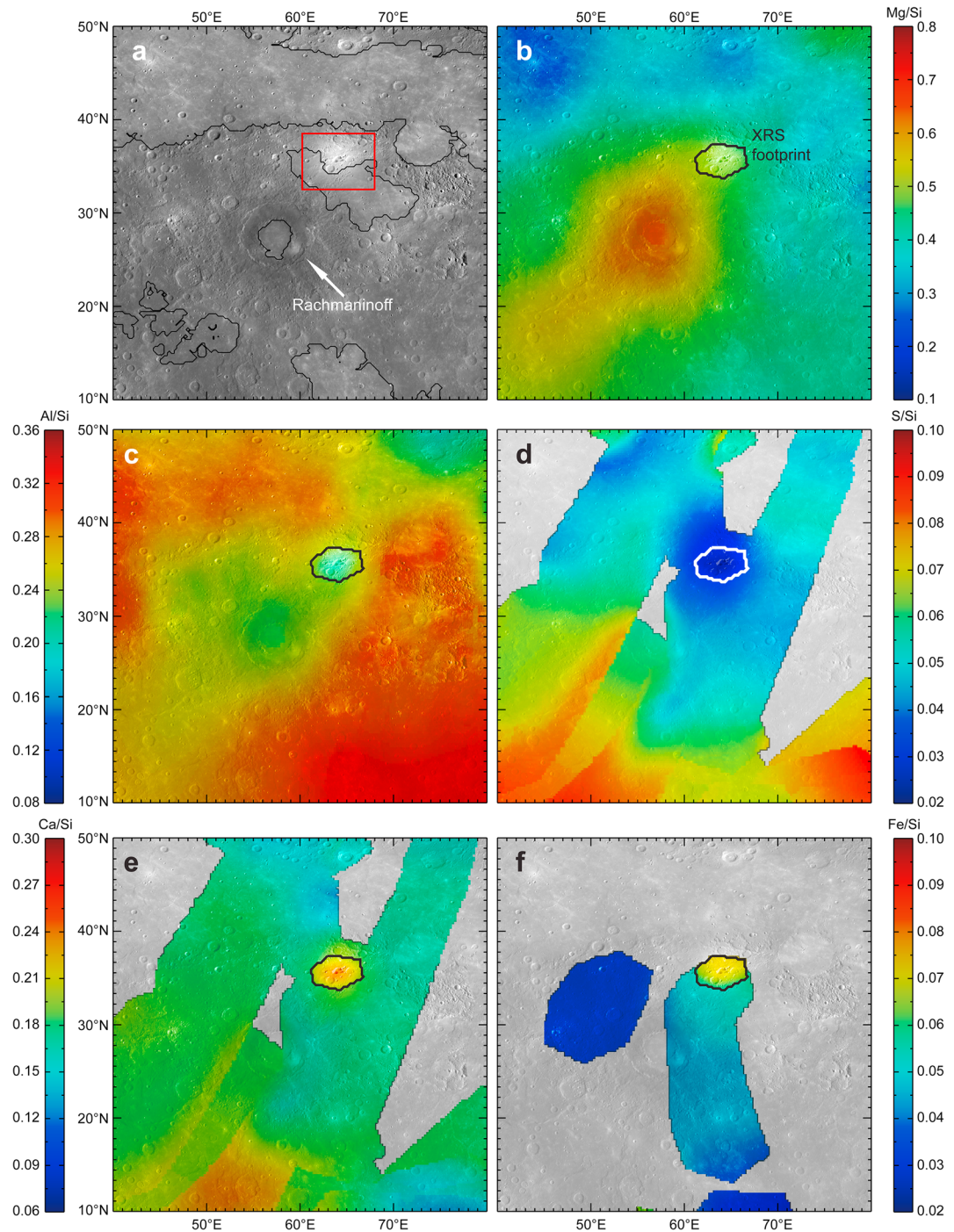
Figure 1. (a) MDIS monochrome base map of the region around the Rachmaninoff basin and the NE Rachmaninoff pyroclastic deposit (bright region within red box). Smooth plains boundaries, as mapped by *Denevi et al.* [2013], are outlined in black. XRS-derived maps for (b) Mg/Si, (c) Al/Si, (d) S/Si, (e) Ca/Si, and (f) Fe/Si, overlaid on the MDIS base map, with the footprint of the targeted XRS observation outlined.

MESSENGER X-Ray Spectrometer (XRS) data for NE Rachmaninoff. We use this information, together with results from MESSENGER's Neutron Spectrometer (NS), Mercury Atmospheric and Surface Composition Spectrometer (MASCS) Visible and Infrared Spectrometer (VIRS), and Mercury Dual Imaging System (MDIS), to constrain the chemical composition of NE Rachmaninoff and offer inferences about the composition and origin of the volatiles involved in the eruption that emplaced the deposit.

Table 1. Details of Targeted XRS Observation of NE Rachmaninoff on 14 December 2013 and Derived Elemental Weight Ratios

Observation Details	
Start time	09:24:50 UTC
Integration period	200 s
Average solar temperature	18.9 MK
Mean incidence angle	59.8°
Mean emission angle	40.0°
Mean phase angle	89.5°
Abundance Ratios[a]	
Mg/Si	0.485 ± 0.011 (0.439)
Al/Si	0.212 ± 0.010 (0.275)
S/Si	0.021 ± 0.003 (0.073)
Ca/Si	0.236 ± 0.004 (0.161)
Ti/Si	0.011 ± 0.002 (0.012)
Fe/Si[b]	0.072 ± 0.007 (0.052)

[a]Ratios are provided with associated fitting errors. Ratios in parentheses represent Mercury's "average" composition, derived from XRS observations of the southern hemisphere [*Weider et al.*, 2014, 2015].
[b]Fe/Si ratio is corrected for a phase-angle effect, following the methodology of *Weider et al.* [2014] (an updated equation is based on the most recent XRS Fe/Si data).

2. Methodology

Through planetary X-ray fluorescence (XRF) spectroscopy, data from MESSENGER's XRS [*Schlemm et al.*, 2007] can be used to quantify the major element composition of Mercury's uppermost (top ~100 μm) crust. Global maps of Mg/Si and Al/Si have been constructed from XRS data [*Weider et al.*, 2015; *Nittler et al.*, 2016]. Maps of S/Si, Ca/Si, and Fe/Si have also been produced, but coverage for those ratios is less complete [*Weider et al.*, 2015; *Nittler et al.*, 2016]. The XRS instrument's 12° field of view (FOV) and variable integration times, coupled with the spacecraft's eccentric orbit, yield measurement "footprints" that vary from <100 km (over high northern latitudes) to >3000 km (over the southern hemisphere) in effective diameter [*Schlemm et al.*, 2007; *Weider et al.*, 2012]. The average spatial resolution of XRS maps thus ranges from ~250 km to almost 2000 km [*Weider et al.*, 2015].

During MESSENGER's second extended mission, several sites of scientific interest were the focus of XRS "targeted observations." During these measurements, the spacecraft was rotated to keep the instrument's FOV centered on a target for up to tens of minutes to maximize the chance of obtaining high-quality XRF data during a solar flare. These measurements were the first from a planetary mission when a geochemical remote sensing instrument dictated spacecraft pointing for feature tracking.

On 14 December 2013, a powerful solar flare occurred during a targeted XRS observation of NE Rachmaninoff. For our analysis, we used only the first five XRS integrations (i.e., 200 s) of the 440-s-long flare (see Table 1). This interval was the most powerful and stable phase of the flare and thus provided spectra with the highest signal-to-noise ratios. We used our standard forward modeling procedure [*Nittler et al.*, 2011; *Weider et al.*, 2012, 2014, 2015], based on the fundamental parameters approach [*Clark and Trombka*, 1997; *Nittler et al.*, 2001], to fit the spectra (Figure S1b in the supporting information) and derive elemental abundance estimates for NE Rachmaninoff. For this analysis, we fit the individual solar spectra (Figure S1a) obtained from the Solar Assembly for X-rays component of XRS [*Schlemm et al.*, 2007]. Following the methods of *Weider et al.* [2014], we then calculated an intensity-weighted average solar flare plasma temperature from the five individual spectra, and we used the *CHIANTI* code [*Dere et al.*, 1997] to generate a high-resolution model solar spectrum. In addition to this model solar spectrum, we used the viewing geometry, X-ray scattering information, atomic physics parameters, and an X-ray detector background as inputs for our forward model to obtain theoretical XRS spectra for varying elemental abundances. We compared such model spectra with the observed XRS spectrum (i.e., five coadded measured spectra) and used a nonlinear χ^2 minimization routine to estimate elemental abundances. The mean temperature of the emitting solar plasma for this flare was ~19 MK (Table 1), sufficient to derive abundance ratios for Mg, Al, S, Ca, Ti, and Fe, all relative to Si (Table 1).

3. XRS Results

Our forward modeling results for NE Rachmaninoff (Table 1) are shown in the context of the latest XRS global elemental maps [*Nittler et al.*, 2016] in Figure 1. In our mapping procedure [*Weider et al.*, 2015], the value of each pixel is weighted more heavily by XRS measurements with the smallest footprints and lowest fitting errors. We therefore excluded overlapping (i.e., non-targeted) data within the footprint of the targeted observation, as these would dilute the high signal-to-noise ratio of the measurement. We find that
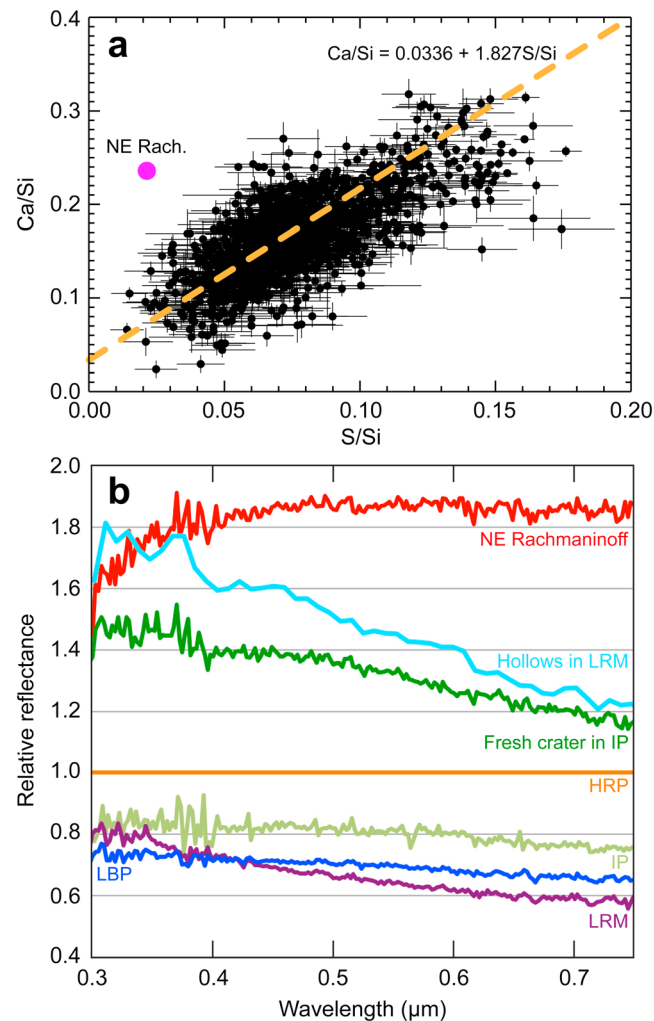
Figure 2. (a) Ca/Si versus S/Si (elemental weight ratios) for each pixel in the global XRS maps. The pink data point indicates NE Rachmaninoff. The equation for the line that best fits the data (dashed orange) is given. (b) MASCS VIRS spectra for NE Rachmaninoff and other Mercury spectral units. Unit nomenclature follows *Murchie et al.* [2015]. To accentuate subtle spectral properties, spectra are normalized to that of high-reflectance red plains (HRP) within the northern lowlands. LRM: low-reflectance material. LBP: low-reflectance blue plains. IP: intermediate plains. The pronounced decrease in relative reflectance at wavelengths shorter than ~0.36 μm in the NE Rachmaninoff spectrum indicates a strong oxygen-metal charge transfer absorption band.

NE Rachmaninoff has similar Mg/Si and Al/Si, but higher Ca/Si, than the immediately surrounding terrain. Although the Fe/Si map indicates that the deposit has a relatively high Fe content, the full regional context cannot be established because of incomplete coverage.

Previous XRS results [*Nittler et al.*, 2011; *Weider et al.*, 2012, 2014, 2015] have shown that there is a ubiquitous positive correlation between the concentrations of S and Ca on Mercury's surface, at all mapped spatial scales. This correlation has been interpreted as evidence for an abundance of Ca-bearing sulfide minerals (e.g., oldhamite) [*Nittler et al.*, 2011; *Weider et al.*, 2012, 2014]. Our targeted XRS results, however, show a striking excursion from this trend (Figure 2a). The S/Si composition of NE Rachmaninoff is lower than in the immediately surrounding areas (Figure 1d) and falls at the low end of the planet's S/Si distribution (Figure 2a). The S/Si ratio of the NE Rachmaninoff deposit (0.02) is much lower than would be expected on the basis of its Ca/Si value of 0.24 (the expected S/Si is ~0.11). Indeed, NE Rachmaninoff has by far the highest mapped Ca/S ratio on Mercury's surface (about 5 times higher than the global mean; Figure S2).

4. Discussion

Mercury's pyroclastic deposits are an end-member within MDIS and MASCS ultraviolet to near-infrared spectral reflectance data (Figure 2b), in that they are typified by high reflectance and red spectral slopes [*Blewett et al.*, 2009; *Izenberg et al.*, 2014; *Murchie et al.*, 2015]. The low reflectance of fresh craters on Mercury, compared with those on the Moon, indicates that Mercury's surface material contains an abundant opaque phase not present in the lunar regolith [*Denevi and Robinson*, 2008; *Braden and Robinson*, 2013]. Among spectral classes of Mercury's surface materials, it is thought that low-reflectance material (LRM) contains the highest concentration of this opaque phase [*Robinson et al.*, 2008]. The heterogeneous distribution of this ubiquitous darkening agent accounts for differences in reflectance across Mercury's surface [*Denevi et al.*, 2009], but there has been much discussion regarding its composition, and several candidate materials have been proposed. A Ti-bearing mineral (e.g., ilmenite) as the darkening phase [*Robinson et al.*, 2008] is ruled out on the basis of Mercury's low Ti content and reduced nature [*Nittler et al.*, 2011; *Zolotov et al.*, 2013; *Weider et al.*, 2014]. Sulfides (e.g., CaS, MgS, and FeS) have also previously been suggested [*Blewett et al.*, 2013; *Helbert et al.*, 2013], but these alone cannot account for the required reduction in reflectance [*Murchie et al.*, 2015].

Graphite is another candidate opaque material on Mercury [*Denevi et al.*, 2009; *Bruck Syal et al.*, 2015]. Indeed, from modeling MDIS data, *Murchie et al.* [2015] showed that 1–5 wt % graphite can account for the low reflectance of LRM. This hypothesis is supported by low-altitude NS measurements, which indicate enhanced thermal neutron emissions over three sampled LRM deposits [*Peplowski et al.*, 2016]. These NS data are sensitive to the total (macroscopic) neutron-absorption cross section of materials within the top ~1 m of Mercury's surface. By attributing the change in the thermal neutron signal (which is especially sensitive to high-absorption and low-absorption elements such as Fe and C, respectively) to C, *Peplowski et al.* [2016] estimated that Mercury's LRM deposits contain 1–3 wt % more C than surrounding, higher-reflectance regions. Additional low-altitude (<200 km) NS data were used to assess the composition of a 600×600 km region centered on NE Rachmaninoff. *Peplowski et al.* [2016] found a $1.4 \pm 0.8\%$ relative decrease in thermal neutron count rate for the measurements that sampled the pyroclastic deposit, and they attributed this difference to a 1–2 wt % depletion in C from that of the surrounding region.

An examination of VIRS reflectance data (300–1450 nm) indicates little spectral contrast across Mercury's surface [*Izenberg et al.*, 2014]. To enhance subtle spectral features (see Figure 2b), the reflectance data are thus typically normalized to a reference area (e.g., high-reflectance red plains in Mercury's northern lowlands) [*Murchie et al.*, 2015]. Furthermore, according to *Izenberg et al.* [2014], there is no region on Mercury >20 km across that exhibits a 1 μm crystal-field absorption (which would be indicative of ≥ 1 wt % Fe^{2+} within silicates) [*Klima et al.*, 2011]. However, nearly all of Mercury's pyroclastic deposits (including NE Rachmaninoff) exhibit an oxygen-metal charge transfer (OMCT) absorption band [*Goudge et al.*, 2014]. This OMCT band (typically centered at ~0.2–0.3 μm) is much stronger than the 1 μm band and is easily detected for Fe^{2+} contents <0.1 wt %. For larger (yet <1 wt %) FeO contents, however, the OMCT band is so strong that light at, and near, its center wavelength is absorbed and the band itself is indistinct ("saturated") [*Cloutis et al.*, 2008]. In VIRS spectra of pyroclastic deposits the band is seen as a downturn at wavelengths less than ~0.36 μm, but it is not detected in spectra from any other surface unit (Figure 2b). On the basis of the OMCT band strength in pyroclastic deposits [*Goudge et al.*, 2014], we estimate that NE Rachmaninoff (with Mercury's highest reflectance) contains ~0.03–0.1 wt % FeO. Non-detection of the OMCT band from other materials could be the result of Fe^{2+} contents closer to ~1 wt %, i.e., so that the band is saturated.

Pyroclastic eruptions are driven by the expansion of volatiles exsolved from the magma during ascent [e.g., *Wilson and Head*, 1981]. At the extremely reducing conditions of Mercury's interior (fO_2 2.6–7.3 $\log_{10}$ units below the iron-wüstite buffer [*McCubbin et al.*, 2012; *Zolotov et al.*, 2013]), S, Cl, and N should be highly soluble in magma, and there should be low abundances of hydrous species [*Zolotov*, 2011]. It has been suggested, however, that oxidation of S, C, N, and Cl melt complexes in ascending magmas (via reaction with oxides) can drive the necessary degassing [*Zolotov*, 2011]. Although orbital observations of Mercury have shown that surface materials are poor in FeO [*Nittler et al.*, 2011; *Evans et al.*, 2012; *Klima et al.*, 2013; *Weider et al.*, 2014], *Zolotov* [2011] noted that some oxidation might be facilitated by reaction with SiO_2-rich (intermediate) rocks. Indeed, the geochemical diversity of Mercury's crust is indicative of mantle heterogeneities [*Peplowski et al.*, 2015; *Weider et al.*, 2015] and substantial variation in silica content. *Vander Kaaden et al.* [2015] showed that although Mercury's rocks typically contain at least 50 wt % SiO_2, some materials contain up to ~63 wt % SiO_2. Reaction of oxides with C and sulfides could occur by either of two scenarios consistent with our data: assimilation of C- and S-bearing LRM into oxide-rich magma or assimilation of oxide-rich country rock into C- and S-bearing magma. Pyroclastic deposits are common immediately inside the rim of the Caloris basin [*Murchie et al.*, 2008], which is partially filled by plains of intermediate composition (~58 wt % SiO_2 on a sulfide-free basis) [*Vander Kaaden et al.*, 2015]. The plains are, in turn, underlain by LRM [*Ernst et al.*, 2010, 2015]. This stratigraphy is thus evidence of an association between SiO_2-rich material and LRM with pyroclastic activity elsewhere on Mercury. We note, however, that the SiO_2 content of NE Rachmaninoff is likely substantially lower (~51 wt % SiO_2 [*Vander Kaaden et al.*, 2015]).

We suggest that the physical and chemical characteristics of NE Rachmaninoff are consistent with the *Zolotov* [2011] hypothesis. The XRS and NS data indicate that the deposit is depleted in S and C compared with typical materials on Mercury's surface. These low abundances can be explained by oxidation of graphite and sulfide complexes in a silicate melt during ascent and the subsequent loss of the liberated volatiles. The high

Table 2. Required Magmatic Abundances of Volatile Species for Emplacement of NE Rachmaninoff Pyroclastic Material (130 km Maximum Radial Range)[a]

Volatile Species	Magmatic Abundance (wt %)	Constituent Element Abundance for Each Species (wt %)					
		H	C	N	O	Cl	S
$CO^{\kappa, \zeta}$	3.0		1.3		1.7		
$CO_2{}^{\kappa}$	4.8		1.3		3.5		
$SO_2{}^{\kappa}$	6.8				3.4		3.4
H_2S^{κ}	3.8	0.2					3.6
H_2O^{κ}	2.0	0.2			1.8		
$N_2{}^{\zeta}$	3.0			3.0			
$S_2{}^{\zeta}$	6.9						6.9
$CS_2{}^{\zeta}$	8.1		1.3				6.8
S_2Cl^{ζ}	10.6					3.8	6.8
Cl^{ζ}	3.8					3.8	
$Cl_2{}^{\zeta}$	7.5					7.5	
COS^{ζ}	6.4		1.3		1.7		3.4

[a]Volatile species suggested as present in Mercury's magmas by *Kerber et al.* [2011] and *Zolotov* [2011] are marked κ and ζ, respectively. Abundances are required for each, rather than all, species.

reflectance of NE Rachmaninoff would arise from removal of graphite (the principal darkening phase) as it was consumed during oxidation. The presence of the OMCT band may be the result of an initially higher Fe^{2+} content, close to ~1 wt %, having been reduced to Fe^0 during the oxidation process. Indeed, the oxidation of volatiles is more likely the result of reaction with FeO-rich than SiO_2-rich materials because O is scavenged from FeO before other oxides (and because NE Rachmaninoff does not have an enriched SiO_2 content).

We tested this oxidation hypothesis by evaluating the amount of C and S exsolution required to produce the spatial extent of the NE Rachmaninoff pyroclastic halo. If the original source magma had a Ca/S ratio typical of Mercury's crust (defined by the correlation in Figure 2a), the amount of S lost during the eruption can be estimated. NE Rachmaninoff should therefore have had an original S/Si ratio of ~0.11, in contrast to the measured ratio of ~0.02. This difference in S/Si corresponds to a potential loss of about 2.5 wt % S (given a Si content of 25 wt % [*Nittler et al.*, 2011]). In previous studies of Mercury's pyroclastic deposits [*Kerber et al.*, 2011; *Thomas et al.*, 2014], the magmatic abundances of selected volatiles in the erupting magmas were estimated from the maximum range of emplaced pyroclastic material from the central vents. We have used the latest estimate for the maximum radial range of the NE Rachmaninoff pyroclastic deposit (130 km) and the methods of *Kerber et al.* [2009] to constrain (on the basis of the molecular mass of each gas) the abundances of magmatic volatiles predicted to be present in Mercury's magmas [*Kerber et al.*, 2011; *Zolotov*, 2011] (see Table 2). The "missing" 2.5 wt % S is less than the value given in Table 2, which suggests that exsolution of this amount of S alone would not have been sufficient to create the NE Rachmaninoff halo.

Low-pressure oxidation of graphite could have led to the formation of CO [e.g., *Rutherford and Papale*, 2009]. If the maximum difference in C content between NE Rachmaninoff and the surrounding area (2 wt % [*Peplowski et al.*, 2016]) was the amount of C that was oxidized and lost from the magma, we can estimate the level of C exsolution that occurred during the eruption (e.g., loss of 2 wt % C is equivalent to exsolution of 4.7 wt % CO). According to the values in Table 2, this amount is more than sufficient to form the deposit. Alternatively, 2 wt % C could yield 3 wt % CS_2 or 4.7 wt % COS, but both these abundances are limited by the availability of 2.5 wt % S and are below the threshold required to drive the pyroclastic activity. The values in Table 2 also show that if N, Cl, or H were the main species responsible for the explosive volcanism, magmatic abundances of 3 wt % N (as N_2), 3.8 wt % Cl (as Cl or S_2Cl), or 0.2 wt % H (as H_2S or H_2O) would have been required. For Cl and H, these concentrations are far in excess of their maximum estimated abundances (0.35 wt % Cl, 50 ppm H) on Mercury's surface [*Evans et al.*, 2015; *Peplowski et al.*, 2015] (there is no evidence for N detection in GRS spectra, indicating a maximum abundance of 1 wt %). It is thus unlikely that N, Cl, or H played a substantial role in the pyroclastic activity. On the basis of all the evidence, we therefore propose that oxidation of graphite and sulfides in the subsurface magma, by reaction with oxides (i.e., FeO and SiO_2), and the subsequent exsolution of C- and S-bearing volatiles during ascent, was responsible for the NE Rachmaninoff eruption.

Mercury's near-surface tectonics have been governed by horizontal compressive stresses for most of the planet's history [e.g., *Byrne et al.*, 2014]. In such a tectonic regime, i.e., dominated by global contraction, it would have been difficult for ascending magmas to reach the surface and drive explosive volcanic eruptions. Magma would have been able to erupt explosively at the surface only if there were sufficient buildup of exsolved gas. Mercury's explosive volcanic vents tend to be located along major fold and thrust belts [*Byrne et al.*, 2014] and around large impact basins. It has thus been suggested that faults and fractures helped facilitate the rise of magmas on Mercury and acted as conduits for positively buoyant melts [*Head and Wilson*, 1992; *Thomas et al.*, 2014]. Although the NE Rachmaninoff vent is not associated with an impact crater, a fault within 100 km may have provided tectonic control on the vent's location [*Habermann and Klimczak*, 2015]. During subsurface storage of the NE Rachmaninoff magma, fractional crystallization of volatile-poor minerals may have led to increased concentrations of volatiles in the remaining melt [e.g., *Bower and Woods*, 1997] until a point at which the volatile overpressure exceeded the confining pressure and the eruption was triggered. Moreover, many of Mercury's pyroclastic deposits are associated with impacts that exposed LRM [*Thomas et al.*, 2015]. Incorporation of C- and/or S-rich LRM wall rock during subsurface storage may therefore have provided an additional source of volatiles within the magma chamber [*Thomas et al.*, 2015].

5. Conclusion

MESSENGER geochemical and spectral reflectance measurements provide complementary evidence for the origin of pyroclastic volcanism on Mercury. Results from a targeted XRS observation of Mercury's largest pyroclastic deposit, NE Rachmaninoff, show that it is depleted in S compared with the rest of the planet's surface. Neutron spectroscopy results from the low-altitude phase of the mission indicate that the deposit is also depleted in C. Pyroclastic deposits on Mercury generally have elevated visible-wavelength spectral reflectance, and they are the only surface material to exhibit an OMCT band (evidence for $\sim$0.03–0.1 wt % Fe^{2+}). These results are all consistent with the hypothesis that the explosive eruptions were driven by exsolution of S- and C-bearing volatile species. These volatiles may have originated from oxidation of graphite and sulfides in the subsurface magma as a result of reactions with relatively FeO-rich materials. The high reflectance thus results from consumption of graphite during oxidation. In addition, the OMCT band may constitute evidence for the reduction of much of the magma's initial ($\sim$1 wt %) FeO content during the oxidation process. It is unclear, however, how well NE Rachmaninoff represents Mercury's other pyroclastic deposits. It is the largest of the planet's pyroclastic deposits and also one of a small minority (about 15% of all Mercury's pyroclastic vents) not located within an impact basin. Although NE Rachmaninoff and the smaller deposits are linked by their OMCT bands and high reflectance, it is not possible to perform comparable geochemical analyses for the smaller deposits with MESSENGER datasets. This issue may be addressed by observations to be acquired by the forthcoming BepiColombo mission [*Benkhoff et al.*, 2010].

References

Benkhoff, J., J. van Casteren, H. Hayakawa, M. Fujimoto, H. Laakso, M. Novara, P. Ferri, H. R. Middleton, and R. Ziethe (2010), BepiColombo—Comprehensive exploration of Mercury: Mission overview and science goals, *Planet. Space Sci.*, 58, 2–20.

Blewett, D. T., M. S. Robinson, B. W. Denevi, J. J. Gillis-Davis, J. W. Head, S. C. Solomon, G. M. Holsclaw, and W. E. McClintock (2009), Multispectral images of Mercury from the first MESSENGER flyby: Analysis of global and regional color trends, *Earth Planet. Sci. Lett.*, 285, 272–282.

Blewett, D. T., et al. (2013), Mercury's hollows: Constraints on formation and composition from analysis of geological setting and spectral reflectance, *J. Geophys. Res. Planets*, 118, 1013–1032, doi:10.1029/2012JE004174.

Bower, S. M., and A. W. Woods (1997), Control of magma volatile content and chamber depth on the mass erupted during explosive volcanic eruptions, *J. Geophys. Res.*, 102, 10,273–10,290, doi:10.1029/96JB03176.

Braden, S. E., and M. S. Robinson (2013), Relative rates of optical maturation of regolith on Mercury and the Moon, *J. Geophys. Res. Planets*, 118, 1903–1914, doi:10.1002/jgre.20143.

Bruck Syal, M., P. H. Schultz, and M. A. Riner (2015), Darkening of Mercury's surface by cometary carbon, *Nat. Geosci.*, 8, 352–356.

Byrne, P. K., C. Klimczak, D. A. Williams, D. M. Hurwitz, S. C. Solomon, J. W. Head, F. Preusker, and J. Oberst (2013), An assemblage of lava flow features on Mercury, *J. Geophys. Res. Planets*, 118, 1303–1322, doi:10.1002/jgre.20052.

Byrne, P. K., C. Klimczak, A. M. C. Sengör, S. C. Solomon, T. R. Watters, and S. A. Hauck II (2014), Mercury's global contraction much greater than earlier estimates, *Nat. Geosci.*, 7, 301–307.

Clark, P. E., and J. I. Trombka (1997), Remote X-ray spectrometry for NEAR and future missions: Modeling and analyzing X-ray production from source to surface, *J. Geophys. Res.*, 102, 16,361–16,384, doi:10.1029/97JE01086.

Cloutis, E. A., K. A. McCormack, J. F. Bell III, A. R. Hendrix, D. T. Bailey, M. A. Craig, S. A. Mertzman, M. S. Robinson, and M. A. Riner (2008), Ultraviolet spectral reflectance properties of common planetary minerals, *Icarus*, 197, 321–347.

Denevi, B. W., and M. S. Robinson (2008), Mercury's albedo from Mariner 10: Implications for the presence of ferrous iron, *Icarus*, 197, 239–246.

Denevi, B. W., et al. (2009), The evolution of Mercury's crust: A global perspective from MESSENGER, *Science*, 324, 613–618.

Denevi, B. W., et al. (2013), The distribution and origin of smooth plains on Mercury, *J. Geophys. Res. Planets*, *118*, 891–907, doi:10.1002/jgre.20074.

Dere, K. P., E. Landi, H. E. Mason, B. C. Monsignori Fossi, and P. R. Young (1997), CHIANTI: An atomic database for emission lines, *Astron. Astrophys. Suppl. Ser.*, *125*, 149–173.

Ernst, C. M., S. L. Murchie, O. S. Barnouin, M. S. Robinson, B. W. Denevi, D. T. Blewett, J. W. Head, N. R. Izenberg, S. C. Solomon, and J. H. Roberts (2010), Exposure of spectrally distinct material by impact craters on Mercury: Implications for global stratigraphy, *Icarus*, *209*, 210–223.

Ernst, C. M., et al. (2015), Stratigraphy of the Caloris basin, Mercury: Implications for volcanic history and basin impact melt, *Icarus*, *250*, 413–429.

Evans, L. G., et al. (2012), Major-element abundances on the surface of Mercury: Results from the MESSENGER Gamma-Ray Spectrometer, *J. Geophys. Res.*, *117*, E00L07, doi:10.1029/2012JE004178.

Evans, L. G., et al. (2015), Chlorine on the surface of Mercury: MESSENGER gamma-ray measurements and implications for the planet's formation and evolution, *Icarus*, *257*, 417–427.

Goudge, T. A., et al. (2014), Global inventory and characterization of pyroclastic deposits on Mercury: New insights into pyroclastic activity from MESSENGER orbital data, *J. Geophys. Res. Planets*, *119*, 635–658, doi:10.1002/2013JE004480.

Habermann, M., and C. Klimczak (2015), Tectonic controls on pyroclastic volcanism on Mercury, Abstract P53A-2101, presented at 2015 Fall Meeting, AGU, San Francisco, Calif., 14–18 Dec.

Head, J. W., III, and L. Wilson (1992), Lunar mare volcanism: Stratigraphy, eruption conditions, and the evolution of secondary crusts, *Geochim. Cosmochim. Acta*, *56*, 2155–2175.

Head, J. W., et al. (2008), Volcanism on Mercury: Evidence from the first MESSENGER flyby, *Science*, *321*, 69–72.

Head, J. W., et al. (2009), Volcanism on Mercury: Evidence from the first MESSENGER flyby for extrusive and explosive activity and the volcanic origin of plains, *Earth Planet. Sci. Lett.*, *285*, 227–242.

Head, J. W., et al. (2011), Flood volcanism in the northern high latitudes of Mercury revealed by MESSENGER, *Science*, *333*, 1853–1856.

Helbert, J., A. Maturilli, and M. D'Amore (2013), Visible and near-infrared reflectance spectra of thermally processed synthetic sulfides as a potential analog for the hollow forming materials on Mercury, *Earth Planet. Sci. Lett.*, *369–370*, 233–238.

Izenberg, N. R., et al. (2014), The low-iron, reduced surface of Mercury as seen in spectral reflectance by MESSENGER, *Icarus*, *228*, 364–374.

Kerber, L., J. W. Head, S. C. Solomon, S. L. Murchie, D. T. Blewett, and L. Wilson (2009), Explosive volcanic eruptions on Mercury: Eruption conditions, magma volatile content, and implications for interior volatile abundances, *Earth Planet. Sci. Lett.*, *285*, 263–271.

Kerber, L., J. W. Head, D. T. Blewett, S. C. Solomon, L. Wilson, S. L. Murchie, M. S. Robinson, B. W. Denevi, and D. L. Domingue (2011), The global distribution of pyroclastic deposits on Mercury: The view from MESSENGER flybys 1–3, *Planet. Space Sci.*, *59*, 1895–1909.

Klima, R. L., M. D. Dyar, and C. M. Pieters (2011), Near-infrared spectra of clinopyroxenes: Effects of calcium content and crystal structure, *Meteorit. Planet. Sci.*, *46*, 379–395.

Klima, R. L., et al. (2013), Constraining the ferrous iron content of silicate minerals in Mercury's crust, *Lunar Planet. Sci.*, *44*, Abstract 1602.

McCubbin, F. M., M. A. Riner, K. E. Vander Kaaden, and L. K. Burkemper (2012), Is Mercury a volatile-rich planet?, *Geophys. Res. Lett.*, *39*, L09202, doi:10.1029/2012GL051711.

Murchie, S. L., et al. (2008), Geology of the Caloris basin, Mercury: A view from MESSENGER, *Science*, *321*, 73–76.

Murchie, S. L., et al. (2015), Orbital multispectral mapping of Mercury with the MESSENGER Mercury Dual Imaging System: Evidence for the origins of plains units and low-reflectance material, *Icarus*, *254*, 287–305.

Nittler, L. R., et al. (2001), X-ray fluorescence measurements of the surface elemental composition of asteroid 433 Eros, *Meteorit. Planet. Sci.*, *36*, 1673–1695.

Nittler, L. R., et al. (2011), The major-element composition of Mercury's surface from MESSENGER X-ray spectrometry, *Science*, *333*, 1847–1850.

Nittler, L. R., E. A. Frank, S. Z. Weider, E. Crapster-Pregont, A. Vorburger, R. D. Starr, and S. C. Solomon (2016), Global major-element maps of Mercury updated from four years of MESSENGER X-ray observations, *Lunar Planet. Sci.*, *47*, Abstract 1273.

Peplowski, P. N., et al. (2011), Radioactive elements on Mercury's surface from MESSENGER: Implications for the planet's formation and evolution, *Science*, *333*, 1850–1852.

Peplowski, P. N., et al. (2012), Variations in the abundances of potassium and thorium on the surface of Mercury: Results from the MESSENGER Gamma-Ray Spectrometer, *J. Geophys. Res.*, *117*, E00L04, doi:10.1029/2012JE004141.

Peplowski, P. N., et al. (2014), Enhanced sodium abundance in Mercury's north polar region revealed by the MESSENGER Gamma-Ray Spectrometer, *Icarus*, *228*, 86–95.

Peplowski, P. N., D. J. Lawrence, W. C. Feldman, J. O. Goldsten, D. Bazell, L. G. Evans, J. W. Head, L. R. Nittler, S. C. Solomon, and S. Z. Weider (2015), Geochemical terranes of Mercury's northern hemisphere as revealed by MESSENGER neutron measurements, *Icarus*, *253*, 346–363.

Peplowski, P. N., R. L. Klima, D. J. Lawrence, C. M. Ernst, B. W. Denevi, E. A. Frank, J. O. Goldsten, S. L. Murchie, L. R. Nittler, and S. C. Solomon (2016), Remote sensing evidence for an ancient carbon-bearing crust on Mercury, *Nat. Geosci.*, *9*, 273–276, doi:10.1038/ngeo2669.

Prockter, L. M., et al. (2010), Evidence for young volcanism on Mercury from the third MESSENGER flyby, *Science*, *329*, 668–671.

Rava, B., and B. Hapke (1987), An analysis of the Mariner 10 color ratio map of Mercury, *Icarus*, *71*, 397–429.

Robinson, M. S., and P. G. Lucey (1997), Recalibrated Mariner 10 color mosaics: Implications for Mercurian volcanism, *Science*, *275*, 197–200.

Robinson, M. S., et al. (2008), Reflectance and color variations on Mercury: Regolith processes and compositional heterogeneity, *Science*, *321*, 66–69.

Rutherford, M. J., and P. Papale (2009), Origin of basalt fire-fountain eruptions on Earth versus the Moon, *Geology*, *37*, 219–222.

Schlemm, C. E., II, et al. (2007), The X-Ray Spectrometer on the MESSENGER spacecraft, *Space Sci. Rev.*, *131*, 393–415.

Thomas, R. J., D. A. Rothery, S. J. Conway, and M. Anand (2014), Mechanisms of explosive volcanism on Mercury: Implications from its global distribution and morphology, *J. Geophys. Res. Planets*, *119*, 2239–2254, doi:10.1002/2014JE004692.

Thomas, R. J., D. A. Rothery, S. J. Conway, and M. Anand (2015), Explosive volcanism in complex impact craters on Mercury and the Moon: Influence of tectonic regime on depth of magmatic intrusion, *Earth Planet. Sci. Lett.*, *431*, 164–172.

Vander Kaaden, K. E., F. M. McCubbin, L. R. Nittler, and S. Z. Weider (2015), Petrologic diversity of rocks on Mercury, *Lunar Planet. Sci.*, *46*, Abstract 1364.

Wallace, P. J., T. Plank, M. Edmonds, and E. H. Hauri (2015), Volatiles in magmas, in *The Encyclopedia of Volcanoes*, 2nd ed., edited by H. Sigurdsson et al., pp. 163–183, Academic Press, London.

Weider, S. Z., L. R. Nittler, R. D. Starr, T. J. McCoy, K. R. Stockstill-Cahill, P. K. Byrne, B. W. Denevi, J. W. Head, and S. C. Solomon (2012), Chemical heterogeneity on Mercury's surface revealed by the MESSENGER X-Ray Spectrometer, *J. Geophys. Res.*, *117*, E00L05, doi:10.1029/2012JE004153.

Weider, S. Z., L. R. Nittler, R. D. Starr, T. J. McCoy, and S. C. Solomon (2014), Variations in the abundance of iron on Mercury's surface from MESSENGER X-Ray Spectrometer observations, *Icarus*, *235*, 170–186.

Weider, S. Z., et al. (2015), Evidence for geochemical terranes on Mercury: Global mapping of major elements with MESSENGER's X-Ray Spectrometer, *Earth Planet. Sci. Lett.*, *416*, 109–120.

Whitten, J. L., J. W. Head, B. W. Denevi, and S. C. Solomon (2014), Intercrater plains on Mercury: Insights into unit definition, characterization, and origin from MESSENGER datasets, *Icarus*, *241*, 97–113.

Wilson, L., and J. W. Head III (1981), Ascent and eruption of basaltic magma on the Earth and Moon, *J. Geophys. Res.*, *86*, 2971–3001, doi:10.1029/JB086iB04p02971.

Zolotov, M. Y. (2011), On the chemistry of mantle and magmatic volatiles on Mercury, *Icarus*, *212*, 24–41.

Zolotov, M. Y., A. L. Sprague, S. A. Hauck II, L. R. Nittler, S. C. Solomon, and S. Z. Weider (2013), The redox state, FeO content, and origin of sulfur-rich magmas on Mercury, *J. Geophys. Res. Planets*, *118*, 138–146, doi:10.1029/2012JE004274.